Spectroscopic features of dissolved iodine in pristine and gamma-irradiated nitric acid solutions

Trent R. Graham*, Brandy N. Gartman, Anjelica Bautista,
Lindsay E.I. Irwin, Eden J. Shelby, Danielle L. Saunders, Timothy J. Johnson,
Mark K. Murphy, Nicolas Uhnak*, Andrew M. Ritzmann, and James M. Bowen

Pacific Northwest National Laboratory, Richland, Washington 99352, United States

(*) CORRESPONDING AUTHOR

Email: trent.graham@pnnl.gov
Email: nicolas.uhnak@pnnl.gov

ABSTRACT

While iodine speciation is important for a wide range of nuclear safety activities, understanding the mechanisms of the transformations of iodine between chemical forms and the sensitivity of these transitions to solution conditions and exposure to radiation remains an active area of research. This work curates spectroscopic data from several experimental techniques and establishes their sensitivity and limitations in detecting changes in iodine speciation in both neutral and acidic regimes. The techniques include Raman spectroscopy, Fourier Transform Infrared (FTIR) spectroscopy, ^{127}I NMR spectroscopy, and ultraviolet-visible (UV-Vis) spectroscopy. Analysis of these data indicates that these commonly accessible spectroscopies often have dynamic ranges of measurable concentrations that do not always overlap between all techniques. The experimental techniques are disparately sensitive to iodide, molecular iodine, iodate, and periodate species. Raman, FTIR, and NMR spectra were subsequentially analyzed using two-dimensional correlation analyses to generate high-resolution autocorrelation spectra. The use of these spectroscopies is then extended to tracking acidification-induced and gamma irradiation-induced transformations of dissolved sodium iodide in deionized water and concentrated nitric acid. Both dissolution into nitric acid and irradiation with a gamma source are demonstrated to perturb the iodine speciation promoting their assembly into molecular iodine (I_2) and/or triiodide (I_3^-). While I_2 and I_3^- species are undetectable with FTIR spectroscopy and ^{127}I NMR spectroscopy, the species can be detected with UV-Vis spectroscopy, and in some instances, I_3^- can be detected with Raman spectroscopy in the low wavenumber region. Ultimately, the results of this work provide a path to designing optimal combinations of techniques to detect forms of iodine across a wide range of concentrations and conditions.

1.0 INTRODUCTION

The varied and dynamic speciation of solution-state iodine species, such as molecular iodine (I_2), iodide (I^-), triiodide (I_3^-), iodate (IO_3^-), and periodate (IO_4^-) presents challenges when attempting to capture iodine for emission controls from fission-based medical isotope production facilities (Doll et al., 2014). Existing strategies to populate iodine speciation models relevant to those processes (Kim and Yeon, 2021) involve a wide variety of experimental techniques to measure iodine species in solution including ion-selective electrode measurements (Moriyama et al., 2010), Winkler titrations with thiosulfate solutions (Anderson et al., 1999), UV-vis spectroscopy (Awtrey and Connick, 1951), inductively coupled plasma-atomic emission spectrometry (ICP-AES), atomic absorption spectrometry (AAS), inductively coupled plasma-mass spectrometry (ICP-MS) (Thomas and Burgess, 2017), vibrational spectroscopies such as Raman and infrared spectroscopy (Durig et al., 1965), (with recent advancements in ultrafast techniques (Biró and Csehi, 2022) with extension to gas phase measurements (Felmy et al., 2021)), EXAFS (Svensson and Kloo, 2003; Feiters et al., 2005; Aimoz et al., 2012; McKeown et al., 2015; Abney et al., 2017), GCMS, IC-ICP/MS, ^{127}I NMR spectroscopy (Genser and Connick, 1973), and gamma spectroscopy (François et al., 2007).

Despite the wide range of techniques typically employed for quantification of iodine concentration and spectroscopic characterization of the speciation, studies of chemically-induced or irradiation-induced oxidation of I^- into I_2 often rely predominantly on spectrophotometric analysis of liquid-liquid extractions to determine iodine speciation (Custer and Natelson, 1949; Ovenston and Rees, 1951; Bosland et al., 2011; Youker et al., 2012; Kim and Yeon, 2021). Liquid-liquid extractions facilitate the extraction of I_2 into the organic phase, which reduces the overlap between I^-, I_2, and I_3^-. For liquid-liquid extractions, others have postulated that the use of

simethicone or other low vapor pressure solvents is advantageous for quantifying I_2 versus volatile organic solvents such as chloroform (He et al., 2020). Studies of the mechanism of radiation-induced oxidation of I^- have led to the formalization of reaction pathways, kinetic models, and observation of relatively long-lived radiolytic products, culminating in empirical models that aid in the prediction of the effects of irradiation on iodine speciation (Moriyama et al., 2011; Cripps et al., 2011; Bilbrey et al., 2020). For example, radioactive pathways involving the formation of I_2 from I^- include a reaction with products formed from the radiolysis of water, such as the hydroxyl radical (·OH) (Moriyama et al., 2010; Milenković and Stanisavljev, 2012), with the reaction pathway enhanced in aerated solutions (Sawai et al., 1966). Molecular iodine can then react with I^- to form I_3^- (Jung et al., 2014, 2015). Beyond the transport of I_2 from solution into the atmosphere through gas evolution, additional reaction pathways are present under certain conditions that can contribute to the reactivity of I_2, such as oxidation of iodine with hydrogen peroxide to form iodate (Stanisavljev et al., 2022). We note that iodate formation is also suggested to proceed via reactions of hypoiodus acid (HIO) under certain pH and temperature conditions post ^{60}Co irradiation (Buxton and Sellers, 1985; Gorbovitskaya and Tiliks, 1996).

Despite the identification of these reaction pathways, spectroscopic characterizations of the iodine speciation in solutions before sample manipulations such as solvent extractions are less readily accessible in literature. The primary focus of this work is thus to compare and contrast multiple spectroscopic methods to identify and quantify multiple iodine species, in particular before and after irradiation by a ^{60}Co gamma source to help direct iodine capture efforts for fission gas control during medical isotope production efforts from producers (Brown et al., 2021). This study focuses on the qualification and quantification of I^-, IO_3^-, and IO_4^- using Raman, FTIR, ^{127}I NMR, and ultraviolet-visible (UV-Vis) spectroscopies. The use of a pseudo-orthogonal strategy

87 combining experimental techniques is important in this work because each spectroscopy has
88 strengths and weaknesses in determining iodine speciation.
89
90 **2.0 EXPERIMENTAL METHODS**
91 *2.1 Sample preparation*
92 All reagents were used as received. An array of reference solutions was prepared by
93 dissolving sodium iodide (NaI, Fisher Scientific), sodium iodate ($NaIO_3$, Fisher Scientific), and
94 sodium periodate ($NaIO_4$, >99.8%, Fisher Scientific) into deionized (DI) water (18 MΩ cm). An
95 additional series of NaI samples was prepared to understand the changes in iodine speciation upon
96 dissolution in nitric acid. For these solutions, NaI solutions of 0.01, 0.1, and 1 M were prepared
97 by the dissolution of NaI salt in a 3 M HNO_3 solution prepared from an optima grade, nitric acid
98 stock solution. To study the effects of gamma irradiation on dissolved sodium iodine speciation in
99 DI water, two concentrations of dissolved NaI in water were prepared with concentrations of NaI
100 of 0.1 and 1 M. To study the effects of gamma irradiation on dissolved sodium iodine speciation
101 in 0.5 M HNO_3, dissolved NaI in 0.5 M HNO_3 was prepared with concentrations of NaI of 1 M.
102 The dissolved NaI in 0.5 M HNO_3 samples was irradiated within an hour of preparation; the
103 irradiation procedure is described below.
104 *2.2 Cobalt-60 mediated gamma irradiation*
105 Gamma irradiation was performed using the Radiological Exposures and Metrology
106 (REM) Laboratory at Pacific Northwest National Laboratory which contains an 11000 Ci ^{60}Co
107 irradiator with a collimated geometry. During irradiation, samples for NMR spectroscopy were
108 placed in pressurize-able NMR sample vessels equipped with a J-young valve (Wilmad Labglass),
109 and samples for pH, oxidation-reduction potential (ORP), Raman, FTIR spectroscopy, and UV-

Vis spectroscopy were placed in glass scintillation vials. Samples were sealed with air in their headspace. Based on the exposure time and separation distance of the sample relative to the ^{60}Co gamma source, the first exposure test samples containing 1 M NaI in 0.5 M HNO_3 were exposed to a dose of 5.0 Mrad (equivalent to 50 kGy) for 4.274 hours at the center for each of the liquid volumes. For the second experiment, samples containing either 0.01 M NaI in DI water or 1 M NaI in DI water, in triplicate, were exposed for 165 hours where the final dose was determined to be 70.9 Mrad (709 kGy) at the center of the liquid. The dose values are in terms of Air Kerma.

2.3 Raman spectroscopy

Raman spectra were measured using a Fourier-transform (FT) Raman spectrometer (Bruker MultiRam 27) equipped with a 1064 nm-excitation laser and an internal aperture setting of 3.5 mm. The beamsplitter was silicon coated onto quartz, the Raman detector for the 1064 channel was a liquid N_2-cooled germanium diode, and the spectrometer incorporated a proprietary notch filter to remove the Rayleigh line before the interferometer. The power of the excitation laser was 450 mW and the 180° backscatter configuration was used in all cases. Typically, at least 1000 interferograms were averaged for each sample. They were collected using the forward-backward double-sided acquisition mode and phase-corrected using the power method due to broad interferograms (Williams et al., 2007; Weatherall et al., 2013; Johnson et al., 2018). Data were obtained with the solutions contained in either fused silica sample holders or quartz capillaries.

Additional samples were measured with a Horiba LabRam HR Raman spectrometer installed on an inverted optical microscope (Nikon Ti-E) with a 632.8 nm HeNe laser light source and a 40× objective. Data were collected via a backscattering geometry setup in which the scattered light was returned through the same 40× objective, transmitted through a beam splitter, dispersed through an 1800 g/mm grating, and detected by an EM-CCD detector. The spectral window was

between wavenumbers of 100 – 4000 cm^{-1}. Spectra were typically collected by averaging 10 exposures of 30-second duration.

The Raman spectroscopy data were processed in Excel (Microsoft, version 2108), where the background was approximated with a spline function. The Raman-active bands of select spectra were fit using purely Lorentzian lineshapes using the generalized reduced gradient method to optimize lineshape parameters and minimize the sum of the squared residuals between the data and the fit. Additional processing utilized 2DShige (v1.3, © Shigeaki Morita, Kwansei-Gakuin University, 2004–2005) to extract autocorrelation spectra from the generalized two-dimensional correlation spectra produced from (i) a concentration array of 0.047, 0.094, 18.7 and 32.7 mM $NaIO_4$ in H_2O and (ii) a concentration array of 0.047, 0.094, 18.7 and 32.7 mM $NaIO_3$ using the dissolved IO_4^- and IO_3^- concentration, respectively, as the perturbation variable.

2.4 FTIR spectroscopy

Fourier transform infrared (FTIR) spectroscopy was performed on a Bruker Vertex 80v equipped with a Harrick DiaMaxATR single reflection diamond ATR cell. Samples were loaded directly onto the ATR crystal. Mid-IR spectra were collected by averaging 128 scans with a resolution of 4 cm^{-1} and a range between 600 – 4000 cm^{-1}. A select region of the spectrum spanning between 700 cm^{-1} and 900 cm^{-1} where diagnostic bands of IO_4^- and IO_3^- vibrations occur were processed via subtraction of the baseline via application of a spline function; pure Gaussian lineshapes were then used to fit the data. Regression of the Gaussian lineshape parameters was performed in Excel. Additional processing utilized 2DShige to generate the 2D synchronous correlation spectra and autocorrelation spectra using the concentration of dissolved IO_4^- and IO_3^- as the perturbation variable. Difference FTIR spectra were also calculated via subtraction of an

FTIR spectrum of the matrix background (e.g. an FTIR spectrum of water for samples dissolved in water or an FTIR spectrum of 3 M HNO_3 for samples dissolved in 3 M HNO_3).

2.5 Iodine-127 NMR spectroscopy

Single pulse, direct excitation ^{127}I NMR spectra were collected on an 11.7 T magnetic field NMR spectrometer. At 11.7 T, the Larmor frequency of ^{127}I is 100.063 MHz. The spectra were acquired with an acquisition time of 52.4 ms enumerated with 131072 complex points, a recycle delay of 0.1 s, a sweep width of 1250000 Hz, and 2048 transients. The pulse width of the ^{127}I NMR spectra was approximately 1.5 ± 0.1 μs, which was equivalent to a π/20 pulse width. The chemical shift of the ^{127}I NMR spectra was externally calibrated with a sample of 0.1 M KI in H_2O (δ = 0 ppm) prepared by the dissolution of potassium iodide salt (KI, > 99.0 %, Sigma-Aldrich) in deionized water. Post-acquisition processing was performed in Mestrenova, where the spectra were left shifted by 180 points and 2000 Hz of exponential line broadening was applied. The spectra were extracted to Excel and fit with purely Lorentzian lineshapes. Additional processing utilized 2DShige to generate the 2D synchronous correlation spectra and autocorrelation spectra using the concentration of dissolved I^- and IO_4^- as the perturbation variable.

2.6 Ultraviolet-visible spectroscopy

Ultraviolet-visible (UV–Vis) spectra were measured using an Agilent Cary-100 UV–visible spectrophotometer. The solutions were loaded into a quartz capillary and UV-Vis spectra were acquired between 180 and 800 nm, with a spectral resolution of 2 nm.

2.7 Oxidation-reduction potential measurements

Oxidation-reduction potential (ORP) was measured using a Thermo Scientific™ Orion™ 815600 ROSS™ Combination pH Electrode in tandem with Thermo Scientific™ Orion™ Redox/ORP/Temp Electrodes. The reference solutions were Thermo Scientific™ Orion™ ORP

Standards for Redox/ORP Electrodes.

3.0 RESULTS

3.1 Characterization of pristine (unirradiated) solutions of $NaIO_4$, $NaIO_3$, and NaI in DI water

A series of calibration solutions using NaI, $NaIO_3$, and $NaIO_4$ were used to characterize aqueous I^-, IO_3^-, and IO_4^-. In addition to evaluating the sensitivity of the Raman, FTIR, ^{127}I NMR, and UV-Vis spectroscopies, post-acquisition processing of the Raman, FTIR, and ^{127}I NMR spectra incorporated 2D synchronous correlation analyses where the autocorrelation spectra were extracted and subsequentially deconvoluted. The generation of autocorrelation spectra promotes the resolution of overlapping signals since the peaks narrow considerably (Noda et al., 2000; Ma et al., 2013; Graham et al., 2021).

Figure 1A shows Raman spectra and 2D synchronous correlation Raman spectra generated from analyzing a series of $NaIO_4$ solutions that varied in concentration between 4.7 and 32.7 mM. The IO_4^- oxyanion exhibits two Raman-active bands in the region between 600 and 1000 cm^{-1}, with the sharp band at 791 cm^{-1} assigned to the symmetric stretching (v_1) motion of the IO_4^- ion and the broadband at 850 cm^{-1} assigned to the asymmetric stretching (v_3) of the IO_4^- ion (Chandrabhas and Sood, 1995). These two bands increase in intensity as a function of the dissolved $NaIO_4$ concentration, which is apparent based on the cross-correlations in their respective 2D synchronous correlation spectra. The autocorrelation spectrum is vertically offset below, and the increase in resolution is apparent based on the reduction in the full-width-at-half-maxima relative to the Raman spectra of the concentrated $NaIO_4$ solution. When comparing the autocorrelation spectrum and the Raman spectrum of the 32.7 mM $NaIO_4$ sample, it is apparent that the minor peak assigned to asymmetric stretching (v_1) at 850 cm^{-1} is of lower intensity than the sharp band

at 791 cm^{-1} compared to the Raman spectrum of 32.7 mM $NaIO_4$ shown in **Figure 1C**. The relative intensity of the two bands in the autocorrelation spectra appears to also depend on their relative full-width-at-half-maxima, with the broad v_3 band considerably attenuated relative to the sharp v_1 band.

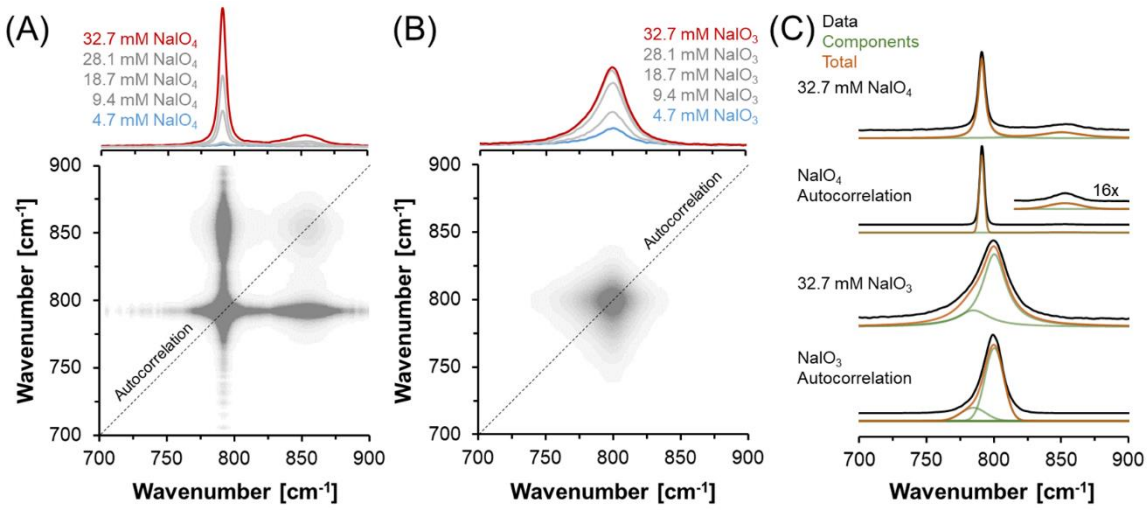

Figure 1. 2D Synchronous correlation Raman spectra acquired with a 1064 nm laser source of (A) $NaIO_4$ dissolved in water and (B) $NaIO_3$ dissolved in water. The 2D spectra are annotated with a dashed line to illustrate the slice used to generate the autocorrelation spectra. (C) Spectral deconvolutions for Raman spectra and the derived autocorrelation spectra for $NaIO_4$ and $NaIO_3$. Note that the 2D synchronous correlation Raman spectra, the spectral deconvolutions of the most concentrated samples, and the autocorrelation spectra are all normalized by their respective, maximum peak height.

Figure 1B displays the Raman spectra and 2D synchronous correlation spectra generated from analyzing a series of $NaIO_3$ solutions that varied in concentration between 4.7 and 32.7 mM. The IO_3^- ion exhibits a slightly asymmetric Raman-active band. Notably, the lineshape of the 2-dimensional peak of the IO_3^- ion is also asymmetric which suggests the presence of a poorly resolved overlapping band. Consequently, the Raman spectrum of dissolved IO_3^- in the region between 600 and 1000 cm^{-1} is best fit by two Lorentzian lineshapes with one centered at 800 cm^{-1} and the other centered at 785 cm^{-1}. These bands are assigned (Durig et al., 1965) to the symmetric

stretching motion (v_1) of the IO_3^- ion at 785 cm^{-1} and antisymmetric stretching motion (v_3) of the IO_3^- ion at 800 cm^{-1}. These bands increase in intensity as a function of the dissolved $NaIO_3$ concentration. The presence of two bands is consistent with prior Raman studies of $NaIO_3$ salts, where bands appear at 789 and 808 cm^{-1}; in this case, the band at lower wavenumbers is assigned to v_1 and the band at higher wavenumbers is assigned to the antisymmetric stretching motion (v_3) of the IO_3^- ion (Durig et al., 1965). As shown in **Figure 1C**, both the Raman spectrum of the 32.7 mM $NaIO_3$ sample and the autocorrelation spectrum can be deconvoluted using two Lorentzian lines. Analysis of the full-width-at-half-maxima of the Raman spectra relative to the autocorrelation spectrum indicates that generation of the autocorrelation spectrum again improves the resolution of the IO_3^- species. Notably, in the case of the two bands in the IO_3^- spectrum, the relative spectral intensities of the IO_3^- bands are more preserved in contrast to the distorted relative spectral intensities of the two IO_4^- Raman-active bands in the autocorrelation spectrum of the IO_4^- sample series.

Figure 2 details the FTIR spectra and 2D synchronous correlation FTIR spectra generated from analyzing a series of $NaIO_4$ or $NaIO_3$ solutions that varied in concentration between 4.7 and 32.7 mM. The IO_4^- oxyanion exhibits asymmetric FTIR-active bands at 842 and 854 cm^{-1} assigned to antisymmetric vibrational modes of the IO_4^- ion via comparison with the Raman spectroscopy data. The IO_3^- oxyanion exhibits an asymmetric FTIR-active band at 800 cm^{-1} assigned to overlapping contributions of the symmetric and antisymmetric stretching motions of the IO_3^- oxyanion.(Durig et al., 1965) For both spectra, the lineshape of the 2-dimensional peaks is quasi-Gaussian but radially asymmetric about the peak maxima, which would suggest the presence of poorly resolved overlapping bands. As shown in **Figure 2C**, both the acquired FTIR spectra of the 32.7 mM $NaIO_4$ sample and $NaIO_3^-$ sample can be deconvoluted with two Gaussian lines. For

either sample, a comparison with the autocorrelation spectra is also shown, and there is a considerable reduction in the full-width-at-half-maxima relative to the original FTIR acquisition.

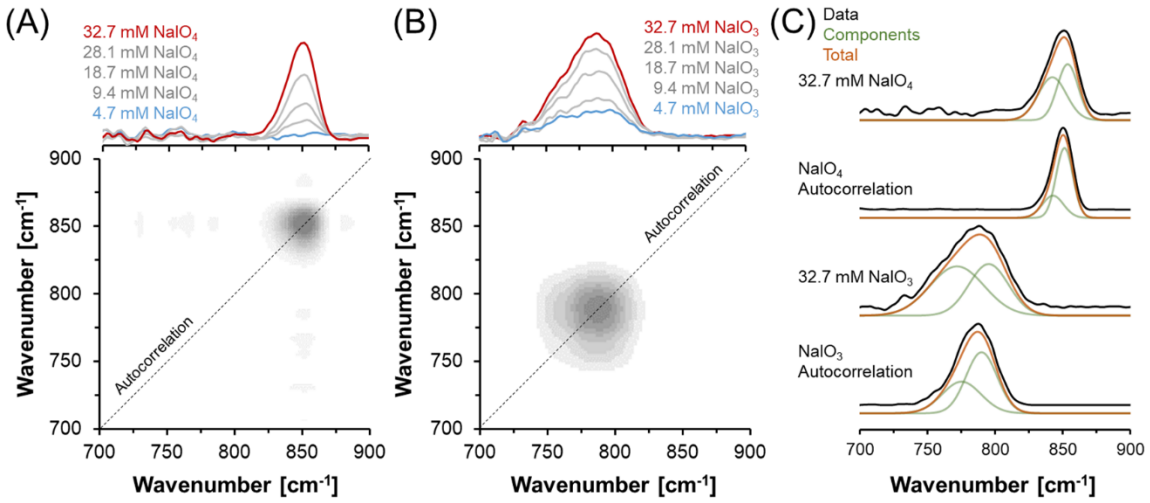

Figure 2. 2D Synchronous correlation FTIR spectra of (A) $NaIO_4$ dissolved in water and (B) $NaIO_3$ dissolved in water. The 2D spectra are annotated with a dashed line to illustrate the slice used to generate the autocorrelation spectra. (C) Spectral deconvolutions for the FTIR spectra and the derived autocorrelation spectra for $NaIO_4$ and $NaIO_3$. Note that the 2D synchronous correlation FTIR spectra, the spectral deconvolutions of the most concentrated samples, and the autocorrelation spectra are all normalized by their respective, maximum peak height.

The results shown in **Figures 1** and **2** demonstrate that either Raman or FTIR spectroscopy can not only detect but can readily discriminate between IO_4^- and IO_3^- based on the appearance and location of the oxyanion vibrational bands. In contrast, dissolved I^- exhibits neither Raman nor IR-active bands. Therefore, ^{127}I NMR and UV-Vis spectroscopy were deployed given that both of the latter spectroscopies are sensitive to dissolved I^-. ^{127}I NMR spectra are shown in **Figure 3**. ^{127}I is quadrupolar (spin 7/2) with very efficient relaxation kinetics. Therefore, the ^{127}I nucleus is not observable in asymmetric environments. Measurable resonances are present for IO_4^- and I^- but not IO_3^-. In **Figure 3A** and **Figure 3B**, the 2D synchronous correlation spectrum is shown for dissolved $NaIO_4$ and NaI, respectively and in either case, the dissolved IO_4^- or I^- concentration is used as the

perturbation variable. Both the IO_4^- and I^- resonance in their respective, 2D synchronous correlation spectra show a single, highly symmetric resonance at 4100 and 0 ppm respectively. As shown in **Figure 3C** and **Figure 3D**, selection of the autocorrelation slice through the $NaIO_4$ or NaI 2D synchronous correlation spectrum generates a spectrum of an increased resolution relative to the 32.7 mM $NaIO_4$ ^{127}I NMR spectrum and 1000 mM NaI spectrum, respectively.

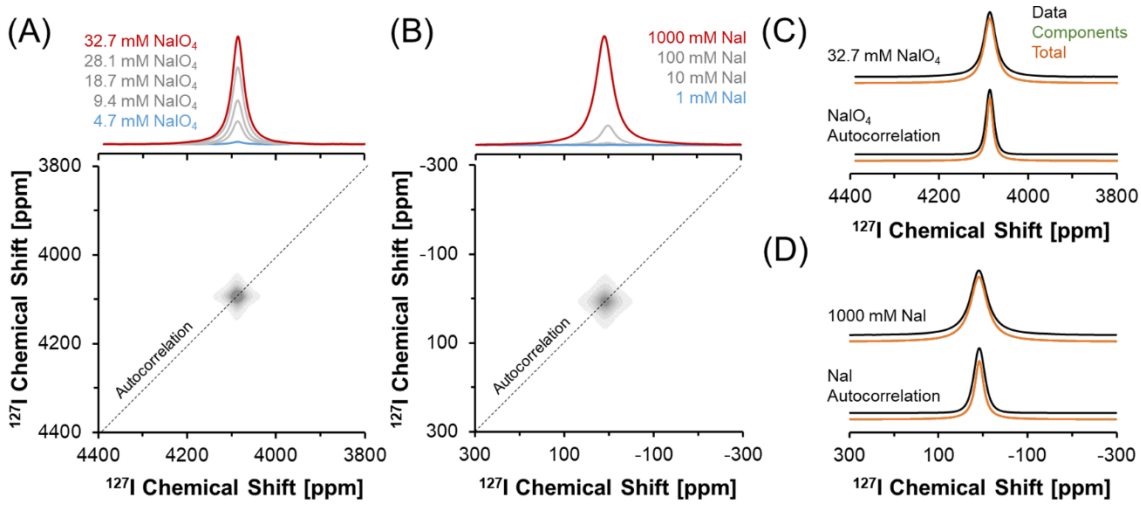

Figure 3. 2D Synchronous correlation ^{127}I NMR spectra of (A) $NaIO_4$ dissolved in water and (B) NaI dissolved in water. The 2D spectra are annotated with a dashed line to illustrate the slice used to generate the autocorrelation spectra. (C) Spectral deconvolutions for ^{127}I NMR spectra and the derived autocorrelation spectra for $NaIO_4$ and NaI. Note that the 2D synchronous correlation ^{127}I NMR spectra, the spectral deconvolutions of the most concentrated samples, and the autocorrelation spectra are all normalized by their respective, maximum peak height.

UV-Vis spectral data are shown in **Figure 4**. Whereas the infrared spectra for $NaIO_4$ and $NaIO_3$ solutions were measured between values of 4.7 and 32.7 mM, the UV-Vis measurements necessitated greater dilutions to avoid saturation of the measured absorbance. Despite being limited to concentrations that are below practical acquisition times for FTIR and Raman, UV-Vis spectroscopy is advantageous because the measurement is sensitive to a broader range of iodine species. Specifically, based on the analysis of literature, I_3^- species are observable with UV-Vis spectroscopy via bands at 284 and 351 nm (Prasanna et al., 2021), I_2 via bands at 461 nm (Prasanna

et al., 2021), IO_4^- at 210 – 230 nm (Valkai et al., 2017), and I^- at 202 nm (Prasanna et al., 2021). Others have deduced that IO^- ions exhibit no signals in UV-Vis spectroscopy in the region between 350 and 500 nm (Kireev et al., 2006). Note that based on analysis of UV-Vis data, there is an ongoing discussion in the literature regarding the IO_4^- speciation across a wide pH range due to possible deprotonation, ortho/meta transformations and dimerization (Buist et al., 1969; Valkai et al., 2017).

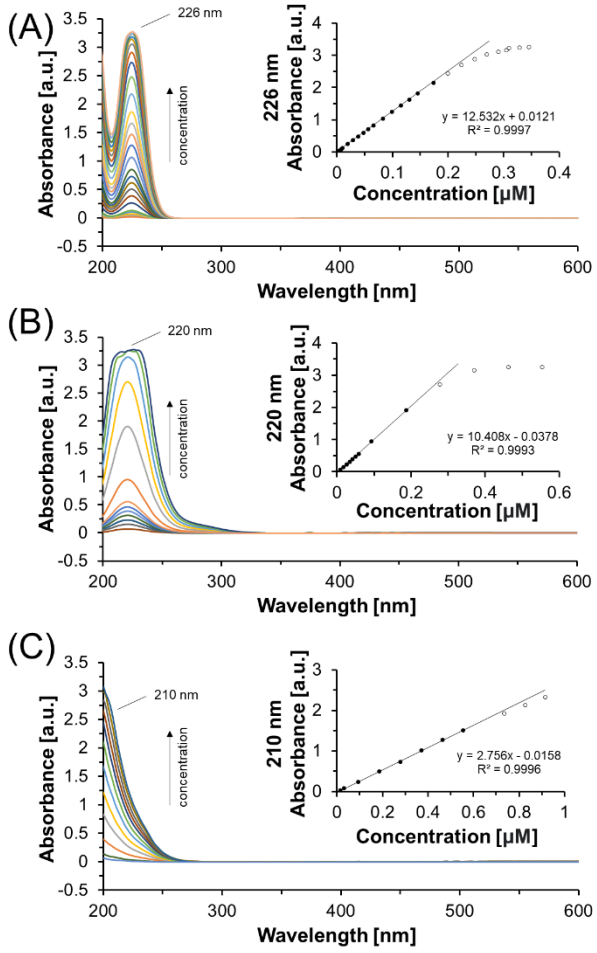

Figure 4. UV-Vis spectroscopy of (A) NaI dissolved in water, (B) $NaIO_4$ dissolved in water, and (C) $NaIO_3$ dissolved in water. The concentration-dependence of the peak height is presented in insets along with a linear regression. The data points used in the linear regression are filled symbols, and the unfilled data points were not used in the linear correlation.

The UV-Vis spectra for the aqueous solutions of NaI, $NaIO_4$, or $NaIO_3$ are shown in **Figure 4**. Solutions containing dissolved NaI and $NaIO_4$ exhibited a resolved peak in the UV-Vis data occurring at 226 and 220 nm, respectively. In contrast, the wavelength of the peak absorbance of solutions of $NaIO_3$ is outside of the UV range, and the absorbance simply decreases exponentially as a function of the wavelength in the UV range. As shown in the insets of **Figure 4**, the solutions exhibited high linearity ($R^2 > 0.999$) across concentration ranges that were unique for the different forms of iodine, and at higher concentrations, the absorbance began to deviate from linearity for all iodine species. Specifically, the absorbance at 226 nm was linear as a function of concentration between 0.002 and 0.173 μM for dissolved NaI, the absorbance at 226 nm was linear as a function of concentration between 0.009 and 0.19 μM for dissolved $NaIO_4$ and the absorbance at 210 nm was linear between 0.02 and 0.65 μM for dissolved $NaIO_3$.

3.2 Characterization of I^- reactivity in ^{60}Co irradiated deionized water

After demonstrating the sensitivity of each spectroscopy to I^-, IO_3^-, and IO_4^-, subsequent series of experiments determined spectroscopy signatures in sodium iodine solutions in DI water irradiated with ^{60}Co. Raman and infrared spectra collected for these samples following gamma irradiation are shown in **Figures S1** and **S2,** respectively. In contrast to the Raman and IR spectra of the dissolved $NaIO_4$ and $NaIO_3$ samples in DI water shown previously in **Figures 1** and **2,** the Raman and IR spectra post-γ-irradiation of NaI do not reveal any spectroscopic signatures of the IO_4^- nor IO_3^- oxyanions, which would be apparent based on the symmetric and asymmetric modes of those ions, respectively. Characterization of the solutions with ^{127}I NMR spectroscopy resulted in the acquisition of spectra without resonances shown in **Figure S3**, which is in contrast to the ^{127}I NMR spectra of dissolved NaI in aqueous solution, where a resonance at 8 ppm assigned to I^- is identifiable in unirradiated solutions. Given the lack of identifiable resonances in the ^{127}I NMR

spectra, and the lack of evidence for IO_3^- and IO_4^- in the Raman and FTIR spectra, we hypothesized that there was either I_2 or I_3^- in these solutions. The chemical environment of the ^{127}I nuclei in I_2 and I_3^- are asymmetric, therefore ^{127}I NMR spectroscopy is not expected to be able to measure those species. To look for evidence of those species, we acquired UV-Vis spectroscopy data after gamma irradiation with a ^{60}Co source.

The UV-Vis data post gamma irradiation of the solutions of dissolved NaI in DI water are shown in **Figure 5** where four peaks are identifiable. A peak assignable to I^- ions occurs at 226 nm, and given the high concentrations, that peak is saturated both in the irradiated and unirradiated samples at 0.01 M and following a 100-fold dilution (performed after irradiation) to 0.0001 M NaI. In the unirradiated, pristine samples at both 0.01 and 0.0001 M, no additional peaks are present, which indicates that only I^- species are found in those solutions.

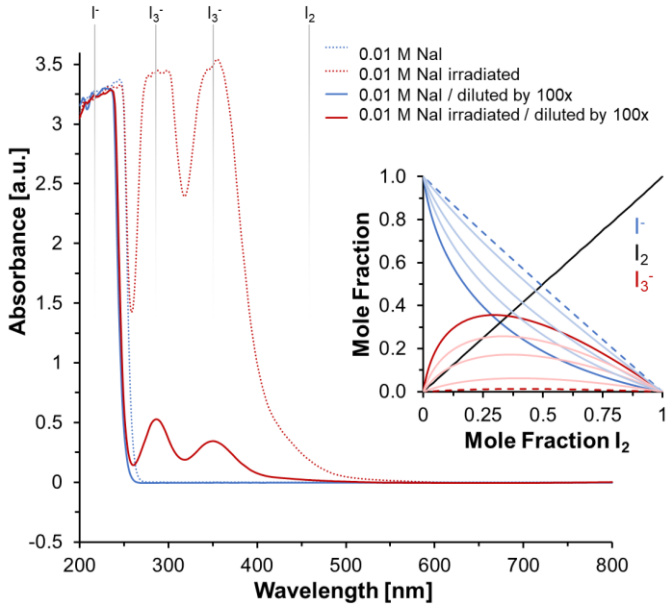

Figure 5. UV-Vis spectroscopy of NaI dissolved in water and a 100x dilution of the NaI solution. Both ^{60}Co and pristine (unirradiated) samples are shown. Given that the irradiated 0.01 M NaI sample saturated observable peaks, the 1 M NaI solution was not analyzed. The approximate peak positions of bands assignable to I^-, I_3^-, and I_2 are annotated to guide the eyes. The inset depicts the relationship between the mole fraction of I^- and I_3^- to variation of the mole

fraction of I_2 and to dilution of the system, indicating that dilution of the irradiated and pristine solutions by a factor of 100x would decrease the relative abundance of I_3^- relative to I_2 and I^-.

As shown in the *Supporting Information*, the effects of dilution can be approximated by using the thermodynamic equilibrium coefficient governing formation of I_3^- as a function of the mole fraction of I_2 and concentration. The equilibrium model is shown in **Scheme 1** and **Equation 1**,

$$I^- + I_2 \overset{K}{\leftrightarrow} I_3^- \qquad \textbf{Scheme S1}$$

where the equilibrium coefficient (K) relates the concentrations, here assumed to be the concentrations, of iodide (C_{I^-}), molecular iodine (C_{I_2}) and triodide ($C_{I_3^-}$) as

$$K = \frac{C_{I_3^-}}{C_{I^-} \cdot C_{I_2}} \qquad \textbf{Equation 1}$$

Others have determined that the equilibrium coefficient (K) to be approximately 700 at 20 °C (Palmer D. A. et al., 1984). The dependence of the mole fraction of iodine species is shown in **Figure 5** at an initial concentration of 10 mM. The lines in blue depict the mole fraction of I^- as a function of I_2, the lines in red show the mole fraction of I_3^- as a function of I_2, and for completeness, the black line shows the mole fraction of I_2 as a function of itself. The speciation at the initial concentration of 10 mM is shown as a solid line, with dilutions of 4-, 16-, and 64-fold shown as light blue and red lines. The dilution factor used in the experiment was 100-fold, which is shown in dashed lines. Analysis of the relationships between the dilution factor and the mole fraction of I^- and I_3^- indicate that I^- is enriched upon dilution at all mole fractions of I_2, whereas the concentration of I_3^- decreases upon dilution at all mole fractions of I_2. Consequentially, in **Figure**

5, if the band attributable to I^- was not saturated, dilution by a factor of 100 would increase the relative intensity of the bands assigned to I^- relative to the bands assigned to I_3^-.

In contrast, the irradiated solutions display additional bands at 351 and 284 nm which are assignable to I_3^- (Prasanna et al., 2021), and a weak shoulder consistent with I_2 at 461 nm (Prasanna et al., 2021). Dilution of the irradiated 0.01 M NaI sample was required to avoid saturation of the band at 351 nm. The UV-Vis spectra shown in **Figure 5** likely contain poorly resolved species beyond I_3^- and I^-, such as oxidation products of I^-. In addition, analysis of the UV-Vis spectra indicates that post ^{60}Co irradiation, there are still abundant I^- ions in the solution which are not observable in the ^{127}I NMR data. The lack of observation of the I^- ions in the ^{127}I NMR data, would imply that the I^- ions are likely undergoing chemical exchange with I_2 and I_3^-. The basis for the presence of I^- in the irradiated solutions of NaI primarily comes from observation of a saturated UV-Vis band near 226 nm. Based on comparison of **Figure 5** with the UV-Vis result in **Figure 4**, the band can be non-uniquely assigned to I^- species. This non-unique assignment is consistent with speciation models, which incorporate a reversible reaction between I^-, I_2, and I_3^-. Since ^{127}I is quadrupolar with very efficient relaxation kinetics, the ^{127}I nucleus is not observable in asymmetric environments, such as in I_2 and I_3^-, and the reaction equilibrium results in a lack of measurable signal in the ^{127}I NMR data. In addition, a concurrent explanation is that the electron field gradients of I^- ions are perturbed by interacting with radiolysis products of water or iodide resulting in an asymmetric environment that is also not measurable with ^{127}I NMR.

Given the possible effects of water radiolysis products on the ^{127}I NMR resonance, oxidation reduction potential (ORP) measurements and pH measurements were collected on the unirradiated and irradiated samples of 0.01 M NaI to understand how dose can influence the water matrix. The pH data indicate that irradiation acidifies the solution, decreasing the pH from 6.67 to

7.06. The ORP data indicate that the irradiation increases the ORP value from 471.4 to 610.2 mV vs. Ag/AgCl. Prior to the irradiation, analysis of the ORP results indicate that the redox active species in solution (i.e. dissolved O_2 and I^-/I_2) are sparse. However, upon irradiation, a number of highly reactive species are produced that are capable of acting upon the I^-/I_2 redox couple or, conversely, be directly responsible for the change in ORP. The radiolytic yields of a given reaction product are quantified using G values, which is defined as the number of species produced or destroyed per 100 eV absorbed. (Elliot et al., 1989) The G values for a neutral pure water system at room temperature determined by Elliot et al. indicate that in neutral water the production of solvated electrons ($e^-_{(aq)}$) and hydroxyl radical (OH) exceeds the production of H_2O_2 by ~3 fold. Roth and LaVerne confirmed the G value while determining H_2O_2 production is independent of pH for pH values spanning between 5 to 9. (Elliot et al, 1989; Roth and LaVerne, 2011) Based on the received dose at room temperature, the predicted concentration of the radiolysis product, H_2O_2, is roughly half of the I^- concentration. Although the UV-Vis indicates that the iodine speciation has changed, the total solution potential found by ORP is likely more dependent on the H_2O_2 redox couple. Several radiolysis products are also acidic, considering the change in pH is on the order of an increase in $[H^+]$ of $\sim 10^{-7}$ M. This falls in line with the general observation that in dilute solutions, the water absorbs nearly all the energy from the impingent gamma radiation. The radiolytic changes in the solution provide conditions that favor the formation of I_3^- as indicated in **Figure 5,** consistent with the observation of others on similar systems (Kim and Yeon, 2021).

For the 1 M NaI samples, the pH and ORP values changed more drastically after receiving dose at room temperature. Irradiation increased the pH of the solution from 7.63 to 11.31 and increased the ORP value from 255.8 to 479.3 ± 0.8 mV. Unlike the lower concentration (0.01 M NaI), the solution became basic. The change in pH can be attributed to a reaction pathway through

which the iodide ion is oxidized to I_2 through oxidation by a radiolytic product of water such as an OH radical under circumneutral conditions ($2I^- + 2OH^\cdot \rightarrow I_2 + 2OH^-$). The oxidation reaction of I^- would then likely proceed until the solution pH approached the pKa of ~11.8 for the OH radical. A similar treatment to that above can be made for the higher I^- concentration, though the concentration difference between the H_2O_2 and I^- is 200-fold. The change in the ORP measurements for the high I^- concentration is likely due to changes in the iodide solution chemistry such as the production of higher-order iodide species. Importantly, the high pH of the 1 M NaI solution results in H_2O_2 reacting as a reductant rather than an oxidant, coupled with a hydrolysis reaction of I_2 to HOI. (Francois et al., 2007)

3.3 Characterization of I^- reactivity in 3 M HNO_3

The reactivity of I^- in concentrated HNO_3 was studied to evaluate the sensitivity of spectroscopies to iodine speciation in conditions relevant to dissolved fission target processes. (Brown et al., 2021) Raman and FTIR spectroscopy of 1 M dissolved NaI salt in 3 M HNO_3 are shown in **Figures S4** and **S5**. Similar to the data acquired from irradiated NaI solutions in deionized water detailed in *Section 3.2*, analysis of the wavenumbers between 600 and 1800 cm^{-1} shown in the Raman and FTIR spectra in **Figures S4** and **S5** do not display any bands attributable to IO_4^- and IO_3^- oxyanions. Instead, the signals in that spectral region only display contributions from dissolved nitric acid (Marcus and Fresco, 1957). Similarly, in the OH-stretching region shown in **Figures S4** and **S5**, there were differences in the OH-stretching band due to the dissolution of increasing concentrations of NaI when comparing the samples of NaI in 3 M HNO_3. ^{127}I NMR spectra are shown in **Figure S6**. No ^{127}I NMR resonances were observable in the ^{127}I NMR spectra, which was hypothesized to be due to the formation of I_2 or I_3^- based on the results

obtained in *Section 3.2* when analyzing ^{60}Co irradiated solutions of NaI in DI water. Therefore UV-Vis spectroscopy was used to look for evidence of I_3^- and I_2 formation after the dissolution of NaI in 3 M HNO_3.

To reduce the saturation effects in the UV-Vis spectra that would be present with a 1 M concentration of NaI in 3 M HNO_3, the UV-Vis spectrum of a solution of 5 μM NaI dissolved in 3 M HNO_3 aged for 1 hour was compared to the matrix of 3 M HNO_3 as shown in **Figure 6**. Inspection of the UV-Vis spectra of 3 M HNO_3 indicates that nitric acid saturates the UV range of the spectrum, preventing observation of I^- which would appear at 226 nm based on the results shown in **Figure 4**. Observing the spectra obtained from 5 μM NaI dissolved in 3 M HNO_3, it is apparent that a trace amount of signal intensity appears at 351 nm, which is consistent with minor amounts of I_3^- in solution. However, the predominant feature in the UV-Vis spectrum is the well-resolved band at 461 nm, which is consistent with I_2 (Prasanna et al., 2021). Others have demonstrated that I^- is oxidized to I_2 by dissolved oxygen in acidic solutions, so it is likely that dissolved oxygen in the solution mediates the transformation of I^- to I_2 as shown in **Figure 6**. (Winkler, 1888; Strickland et al., 1968) Based on these results, the dissolution of NaI into 3 M HNO_3 produces I_2.

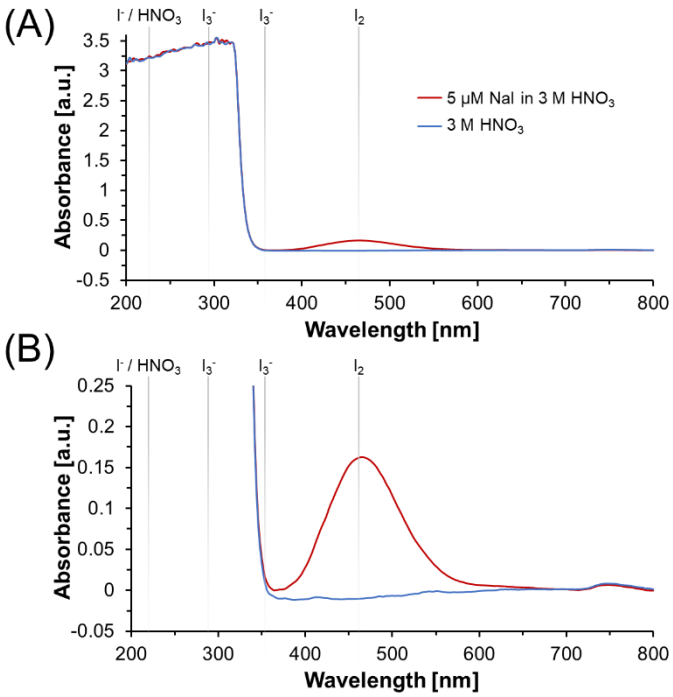

Figure 6. (A) UV-Vis spectroscopy of 5 µM of NaI dissolved in 3 M HNO_3 and comparison with 3 M HNO_3 (B) Vertical magnification of the spectra shown in part A. The approximate peak positions of bands assignable to HNO_3, I^-, I_3^-, and I_2 are annotated to guide the eyes.

414

415 *3.4 Characterization of I^- reactivity in 0.5 M HNO_3 irradiated with ^{60}Co*

416 The effects of ^{60}Co irradiation on dissolved NaI in 0.5 M HNO_3 were also investigated
417 using Raman spectroscopy, FTIR spectroscopy, ^{127}I NMR spectroscopy, and UV-Vis
418 spectroscopy. The Raman and FTIR spectra of 1 M NaI dissolved in 0.5 M HNO_3 are shown in
419 **Figures S7** and **S8**. Similar to the results of ^{60}Co irradiated NaI solutions in DI water and the
420 results from NaI solutions prepared in 3 M HNO_3, detailed in S*ections 3.2* and *3.3*, the Raman and
421 FTIR spectra showed no bands attributable to oxyanions such as IO_3^- nor IO_4^- which would have
422 been apparent based on vibrational modes occurring near 800 cm^{-1} as shown in **Figure 1** and **2**.
423 Data collected by Raman spectroscopy shows a possible variation in the HNO_3 peak (**Figure S7**)
424 between the irradiated and pristine sample, but these changes were not observed in the FTIR
425 spectra (**Figure S8)** and the reduction in intensity occurs coherently with a reduction in the

intensity of the water bending and OH stretching modes. We hypothesize that there may be a change in turbidity due to irradiation, as similar attenuation of Raman signals in turbid samples was observed in nitrogen-based oxyanion samples.(Lines et al., 2022) Notably, the low wavenumber region of the Raman spectra below 300 cm^{-1} displayed two bands that were consistent with I_3^- ions in the solution.(Loos and Jones, 1974) The ^{127}I NMR spectroscopy results shown in **Figure S9** were also similar to the results acquired from ^{60}Co irradiated NaI solutions in DI water and the results from NaI solutions prepared in 3 M HNO_3 in that no ^{127}I NMR resonances were observed in ^{60}Co or pristine, unirradiated solutions of NaI in 0.5 M HNO_3. Based on the UV-Vis spectroscopy results from ^{60}Co irradiated solutions of NaI in deionized water and NaI dissolved in 3 M HNO_3, we hypothesized that the I^- ions had transformed into either I_3^- or I_2.

To discriminate between the possible formation of I_3^- and I_2, UV-Vis spectroscopy was performed, as shown in **Figure 7**. To avoid saturating the detector, a 500-fold dilution was performed such that the I_3^- bands and the I_2 band were observable without saturation effects. As shown in **Figure 7**, both the irradiated and pristine, unirradiated sample display peaks that are attributable to I^- and HNO_3^- at 226 nm, where the absorbance of those species still introduced saturation effects clipping the spectrum. In addition, in both samples, peaks are observable for I_3^- and a weak shoulder is apparent for I_2. The intensities of the peaks are less in the irradiated sample, which is hypothesized to be due to the evaporation of I_2 during the sample irradiation. Notably, the relative intensities of the I_3^- bands at 351 and 284 nm are 1.49 ± 0.01 a.u. when comparing between the irradiated and unirradiated samples, which indicates that the relative intensity of those bands does not change upon ^{60}Co irradiation. This would suggest that both bands are assignable to the I_3^- ion, in agreement with prior literature, and that the formation of I_3^- is independent of the irradiation. (Prasanna et al., 2021) Instead, I_3^- formation is likely an acid-catalyzed reaction, which

is why a 6-fold reduction of HNO_3 concentration from 3 to 0.5 M changes the product from favoring I_2 to I_3^-. Whether I_3^- and I_2 are predominant likely also depends on the redox potential, in addition to the concentration of HNO_3 (pH) (Pourbaix, 1974). Note that the 500-fold dilution would increase the relative abundance of I^- at the expense of I_3^- as shown in the inset. Details of the calculation to relate the mole fraction of I^- and I_3^- to the mole fraction of I_2 and the dilution factor are shown in the *Supporting Information*.

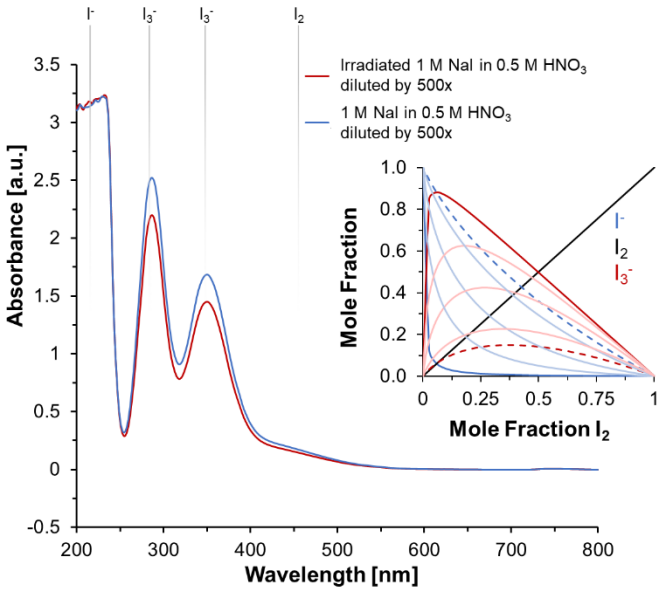

Figure 7. UV-Vis spectroscopy of a 500-fold dilution of 1 M NaI in 0.5 M HNO_3 post gamma irradiation with a ^{60}Co source and comparison with a pristine, unirradiated solution. The approximate peak positions of bands assignable to HNO_3, I^-, I_3^-, and I_2 are annotated to guide the eyes. Note that diluting the irradiated and pristine solutions by a factor of 500x would decrease the relative abundance of I_3^- relative to I_2 and I^-. The inset depicts the effects of 500-fold dilution on the relative mole fractions of I^- and I_3^-. In the inset, the speciation for the undiluted sample is shown in solid lines, dilutions of 16-fold, 64-fold, and 256-fold are shown in light lines, and the 500-fold dilution are shown in dashed lines.

4.0 CONCLUSION

Analysis of the spectroscopy techniques advances our understanding of their sensitivities and limitations in several ways: i) While Raman spectroscopy cannot detect I^- ions, the technique

460 can identify the IO_3^- and IO_4^- oxyanions above concentrations of a few mM. The IO_3^- and IO_4^-
461 oxyanions have distinct line shapes (i.e. full-width-at-half-maxima) and peak positions. For the
462 case of IO_3^- observed with Raman spectroscopy, analysis of synchronous autocorrelation spectra
463 indicates that there are two overlapping bands that were assignable to the symmetric and
464 antisymmetric stretching modes of IO_3^-. While there is some evidence for I_3^- in the low
465 wavenumber region, specialized filters are needed to quantitatively analyze Raman spectra at
466 wavenumbers below 300 cm^{-1}. ii) FTIR spectroscopy can identify the oxyanion IO_3^- and IO_4^- ions
467 but not I^-, I_2, or I_3^-. Identification of IO_3^- and IO_4^- is based on the peak maxima and line shape of
468 the observable bands. Solutions of IO_3^- and IO_4^- can be detected in excess of a few mM with FTIR
469 spectroscopy. For both IO_3^- and IO_4^-, analysis of 2D synchronous autocorrelation spectra indicates
470 the observable bands are composed of at least two peaks, likely attributable to both the symmetric
471 and antisymmetric stretching modes of IO_3^- and IO_4^-. iii) ^{127}I NMR benefits from the isotopic
472 specificity that enables observation of iodine species without the presence of possibly interfering
473 signals from the sample matrix, but the technique's sensitivity is intrinsically limited to forms of
474 iodine with a symmetric local environment such as I^- and IO_4^- species due to the quadrupolar NMR
475 properties of ^{127}I. Following acidification or ^{60}Co irradiation of solutions of dissolved NaI to form
476 either I_2 or I_3^-, no ^{127}I NMR resonance is observable, even when UV-Vis spectroscopy
477 demonstrates that I^- ions are in sufficient quantities to saturate the detector. Therefore, the iodine
478 species are undergoing chemical exchange between I^-, I_2, and I_3^- which results in no observable
479 NMR resonance. iv) UV-Vis spectroscopy can identify I^-, IO_3^-, and IO_4^- in solution in uM
480 quantities, and can also detect the formation of I_3^- and I_2 following ^{60}Co induced gamma irradiation
481 or acidification of DI water with nitric acid. However, even after diluting nitric acid solutions
482 considerably, the absorbance in the UV-Vis range of I^- is saturated by the combined absorbance of

both HNO_3 and I^-. v) Measurements of the matrix conditions to understand redox and pH changes may also provide an understanding of how radiolysis products or mechanisms can influence iodine behavior, which may have real world consequences to the capture of radioiodine for fission based medical isotope producers.

In addition to curating information about the sensitivities and limitations of Raman spectroscopy, FTIR spectroscopy, ^{127}I NMR spectroscopy, and UV-Vis spectroscopy, analysis of the application of these spectroscopies to track iodine speciation in acidified solutions and/or post ^{60}Co induced gamma irradiation provided insight into the changes in iodine speciation. Iodine in the form of dissolved NaI in DI water forms I_3^- ions without the presence of a resolvable UV-Vis band of I_2 post ^{60}Co irradiation. Dissolution of sodium iodide in 0.5 M HNO_3 is observed to form I_3^- and application of ^{60}Co does not perturb the relative UV-Vis line shape of the I_3^- formed from the dissolution of NaI in 0.5 M HNO_3, although changes in the absolute signal intensity were found and attributed to evaporation of volatile I_2 during irradiation. Upon increasing the concentration of nitric acid to 3 M HNO_3, I_2 is observed to form in solutions of dissolved NaI. These studies indicate that of the explored spectroscopies, UV-Vis spectroscopy should be considered the principal method of discriminating irradiation and acidification-induced changes in I^- speciation into I_2 or I_3^-, with the caveat that the presence of HNO_3 saturates the UV range of the UV-Vis spectra. Future work will expand the list of samples beyond monomeric forms of iodine (e.g. I^-, IO_4^- and IO_3^-) to include I_3^- and other forms of iodine (e.g. HIO).

5.0 ACKNOWLEDGEMENTS

This work was funded under the National Nuclear Security Administration's (NNSA) Office of Conversion (NA-231). Raman spectroscopy, FTIR spectroscopy, UV-Vis spectroscopy,

and NMR spectroscopy were performed using facilities at the Environmental Molecular Science Laboratory (EMSL, grid.436923.9), a DOE Office of Science User Facility sponsored by the Office of Biological and Environmental Research at Pacific Northwest National Laboratory (PNNL). PNNL is a multiprogram national laboratory operated for DOE by Battelle Memorial Institute operating under Contract No. DE AC05-76RL0-1830.

6.0 AUTHOR CONTRIBUTION STATEMENT

BNG, NU, AMR, and JMB acquired funding for the work. TRG, BNG, NU, AMR, and JMB designed experiments. TRG, BNG, AB, LEII, and EJS prepared samples. MKM irradiated samples and performed dose calculations. TRG, BNG, AB, DLS, and TJJ performed spectroscopy measurements and solution characterization. TRG interpreted, processed, and analyzed the data. TRG wrote the first draft of the manuscript. TRG, BNG, TJJ, MKM, NU, and AMR edited the manuscript. All authors approved the final manuscript contents.

7.0 WORKS CITED

Abney C. W., Nan Y. and Tavlarides L. L. (2017) X-ray Absorption Spectroscopy Investigation of Iodine Capture by Silver-Exchanged Mordenite. *Ind. Eng. Chem. Res.* **56**, 4837–4846.

Aimoz L., Wieland E., Taviot-Guého C., Vespa M. and Dähn R. (2012) Iodine K-Edge Exafs Spectroscopy of Iodine-Bearing AFm-(Cl_2, CO_3, SO_4). In *Proceedings of the 10th International Congress for Applied Mineralogy (ICAM)* Springer Berlin Heidelberg, Berlin, Heidelberg. pp. 1–7.

Anderson G. L., Andreae O. M., Behrends B. and Al. E. (1999) *Methods of Seawater Analysis*., Wiley.

Awtrey A. D. and Connick R. E. (1951) The Absorption Spectra of I_2 , I_3^- , I^- , IO_3^- , S_4O_6= and S_2O_3= . Heat of the Reaction $I_3^- = I_2 + I^-$. *J. Am. Chem. Soc.* **73**, 1842–1843.

Bilbrey J. A., Marrero C. O., Sassi M., Ritzmann A. M., Henson N. J. and Schram M. (2020) Tracking the Chemical Evolution of Iodine Species Using Recurrent Neural Networks. *ACS Omega* **5**, 4588–4594.

Biró L. and Csehi A. (2022) Tracing the vibrational dynamics of sodium iodide via the spectrum

of emitted photofragments. *Phys. Chem. Chem. Phys.* **24**, 13234–13244.

Bosland L., Funke F., Langrock G. and Girault N. (2011) PARIS project: Radiolytic oxidation of molecular iodine in containment during a nuclear reactor severe accident: Part 2. Formation and destruction of iodine oxides compounds under irradiation – Experimental results modelling. *Nucl. Eng. Des.* **241**, 4026–4044.

Brown, A.M., Johnson, N., Gelis, A. V., Stika, M., Servis, A. G., Bakken, A., Krizmanich, C., Shannon, K., Kozak, P., Barnhart, A., Denbrock, C., Luciani, N., Grimm, T. and Tkac, P. (2021) Recovery of high specifica activity molbdenum-99 from accelerator-induced fission on low-enriched uranium for technetium-99m generators. *Sci. Rep.* **11,** 13292.

Buist G. J., Hipperson W. C. P. and Lewis J. D. (1969) Equilibria in alkaline solutions of periodates. *J. Chem. Soc. A Inorganic, Phys. Theor.*, 307.

Buxton G. V. and Sellers R. M. (1985) Radiation-induced redox reactions of iodine species in aqueous solution. Formation and characterisation of III, IIV, IVI and IVIII, the stability of hypoiodous acid and the chemistry of the interconversion of iodide and iodate. *J. Chem. Soc. Faraday Trans. 1 Phys. Chem. Condens. Phases* **81**, 449.

Chandrabhas N. and Sood A. K. (1995) Raman study of pressure-induced phase transitions in $RbIO_4$. *Phys. Rev. B* **51**, 8795–8800.

Cripps R. C., Jäckel B. and Güntay S. (2011) On the radiolysis of iodide, nitrate and nitrite ions in aqueous solution: An experimental and modelling study. *Nucl. Eng. Des.* **241**, 3333–3347.

Custer J. J. and Natelson S. (1949) Spectrophotometric Determination of Microquantities of Iodine. *Anal. Chem.* **21**, 1005–1009.

Doll C. G., Sorensen C. M., Bowyer T. W., Friese J. I., Hayes J. C., Hoffmann E. and Kephart R. (2014) Abatement of xenon and iodine emissions from medical isotope production facilities. *J. Environ. Radioact.* **130**, 33–43.

Durig J. R., Bonner O. D. and Breazeale W. H. (1965) Raman Studies of Iodic Acid and Sodium Iodate. *J. Phys. Chem.* **69**, 3886–3892.

Elliot A.J., Chenier, M.P. and Oullette, D.C. (1990) g-Values for γ-irradiated water as a function of temperature. *Can. J. Chem.* **68,** 712-719.

Feiters M. C., Küpper F. C. and Meyer-Klaucke W. (2005) X-ray absorption spectroscopic studies on model compounds for biological iodine and bromine. *J. Synchrotron Radiat.* **12**, 85–93.

Felmy H. M., Clifford A. J., Medina A. S., Cox R. M., Wilson J. M., Lines A. M. and Bryan S. A. (2021) On-Line Monitoring of Gas-Phase Molecular Iodine Using Raman and Fluorescence Spectroscopy Paired with Chemometric Analysis. *Environ. Sci. Technol.* **55**, 3898–3908.

François A., Ball J., Bosland L., Bernard C., Dickinson S., G D., Guilbert S., Herranz L. E. and Jacquemain D. (2007) *Radiolytic oxidation of iodine in the containment at high temperature and dose rate*.

Genser E. E. and Connick R. E. (1973) Exchange of iodide ion with triiodide ion studied by nuclear magnetic resonance. *J. Chem. Phys.* **58**, 990–996.

Gorbovitskaya T. and Tiliks J. (1996) *The effect of temperature on radiolysis of iodide ion diluted aqueous solutions*., Switzerland.

Graham T. R., Dembowski M., Wang H.-W., Mergelsberg S. T., Nienhuis E. T., Reynolds J. G., Delegard C. H., Wei Y., Snyder M., Leavy I. I., Baum S. R., Fountain M. S., Clark S. B., Rosso K. M. and Pearce C. I. (2021) Hydroxide promotes ion pairing in the $NaNO_2$ –NaOH – H_2O system. *Phys. Chem. Chem. Phys.* **23**, 112–122.

He S., Chen Q., Ao X., Li C., Yu M. and Zuo Y. (2020) A method for the removal of trace iodine from wet-process phosphoric acid. *Hydrometallurgy* **191**, 105208.

Johnson T. J., Su Y.-F., Bryan S. A., Sweet L. E., Corbey J. F. and Tonkyn R. G. (2018) Characterization of uranium ore concentrate chemical composition via Raman spectroscopy. In *Chemical, Biological, Radiological, Nuclear, and Explosives (CBRNE) Sensing XIX* (eds. A. W. Fountain, J. A. Guicheteau, and C. R. Howle). SPIE. p. 15.

Jung S.-H., Yeon J.-W., Hong S. Y., Kang Y. and Song K. (2015) The Oxidation Behavior of Iodide Ion Under Gamma Irradiation Conditions. *Nucl. Sci. Eng.* **181**, 191–203.

Jung S.-H., Yeon J.-W., Kang Y. and Song K. (2014) Determination of Triiodide Ion Concentration Using UV-Visible Spectrophotometry. *Asian J. Chem.* **26**, 4084–4086.

Kim M. and Yeon J.-W. (2021) Accuracy analysis on concentration determination of molecular iodine in gamma irradiated solutions. *J. Radioanal. Nucl. Chem.* **330**, 469–473.

Kireev S. V., Kuzema A. V., Simanovskiĭ I. G. and Shnyrev S. L. (2006) An absorption method of detecting iodine-containing substances in liquid alkaline media formed during nuclear reprocessing. *Opt. Spectrosc.* **100**, 403–408.

Lines A. M., Bello J. M., Gasbarro C. and Bryan S. A. (2022) Combined Raman and Turbidity Probe for Real-Time Analysis of Variable Turbidity Streams. *Anal. Chem.* **94**, 3652–3660.

Loos K. R. and Jones A. C. (1974) Structure of triiodide ion in solution. Raman evidence for the existence of higher polyiodide species. *J. Phys. Chem.* **78**, 2306–2307.

Ma L., Sikirzhytski V., Hong Z., Lednev I. K. and Asher S. A. (2013) Insight into Resolution Enhancement in Generalized Two-Dimensional Correlation Spectroscopy. *Appl. Spectrosc.* **67**, 283–290.

Marcus R. A. and Fresco J. M. (1957) Infrared Absorption Spectra of Nitric Acid and Its Solutions. *J. Chem. Phys.* **27**, 564–568.

McKeown D. A., Muller I. S. and Pegg I. L. (2015) Iodine valence and local environments in borosilicate waste glasses using X-ray absorption spectroscopy. *J. Nucl. Mater.* **456**, 182–191.

Milenković M. C. and Stanisavljev D. R. (2012) Role of Free Radicals in Modeling the Iodide–Peroxide Reaction Mechanism. *J. Phys. Chem. A* **116**, 5541–5548.

Moriyama K., Maruyama Y. and Nakamura H. (2011) *Kiche: A simulation tool for kinetics of iodine chemistry in the containment of light water reactors under severe accident conditions (Contract research)*., Japan.

Moriyama K., Tashiro S., Chiba N., Hirayama F., Maruyama Y., Nakamura H. and Watanabe A. (2010) Experiments on the Release of Gaseous Iodine from Gamma-Irradiated Aqueous CsI Solution and Influence of Oxygen and Methyl Isobutyl Ketone (MIBK). *J. Nucl. Sci. Technol.* **47**, 229–237.

Noda I., Dowrey A. E., Marcott C., Story G. M. and Ozaki Y. (2000) Generalized Two-Dimensional Correlation Spectroscopy. *Appl. Spectrosc.* **54**, 236A-248A.

Ovenston T. C. J. and Rees W. T. (1951) Note on the spectrophotometric determination of iodine by extraction with organic solvents. *Anal. Chim. Acta* **5**, 123–127.

Palmer D. A., Rametrte R. W. and Mesmer R. E. (1984) Triiodide Ion Formation Equilibrium and Activity Coefficients in Aqueous Solution. *J Solution Chem.* **13**, *673*–683.

Pourbaix M. (1974) *Atlas of Electrochemical Equilibria in Aqueous Solutions*. 2nd ed., National Association of Corrosion Engineers.

Prasanna, Shrikanth B. K. and Hegde M. S. (2021) Formation and Structure of Iodine: Water (H_2O-I_2) charge-transfer complex. *J. Chem. Sci.* **133**, 51.

Roth O. and LaVerne, J.A. (2011) Effect of pH on H_2O_2 Production in the Radiolysis of Water. *J. Phys. Chem. A.* **115,** 700-708.

Sawai T., Shinozaki Y. and Meshitsuka G. (1966) The Radiolysis of Aqueous Solutions of Potassium Iodide. *Bull. Chem. Soc. Jpn.* **39**, 951–955.

Stanisavljev D., Taylor A. F. and Bubanja I. N. (2022) Coupling between nucleation and chemical reactions and its importance in understanding the oxidation of iodine by hydrogen peroxide. *Phys. Chem. Chem. Phys.* **24**, 14022–14032.

Strickland, J.D.H., and Parsons, T.R. (1968). Determination of dissolved oxygen. In A Practical Handbook of Seawater Analysis. Fisheries Research Board of Canada, Bulletin, 167, 71–75.

Svensson P. H. and Kloo L. (2003) Synthesis, Structure, and Bonding in Polyiodide and Metal Iodide−Iodine Systems. *Chem. Rev.* **103**, 1649–1684.

Thomas O. and Burgess C. (2017) *UV-Visible Spectrophotometry of Water and Wastewater*.,

Valkai L., Peintler G. and Horváth A. K. (2017) Clarifying the Equilibrium Speciation of Periodate Ions in Aqueous Medium. *Inorg. Chem.* **56**, 11417–11425.

Weatherall J. C., Barber J., Brauer C. S., Johnson T. J., Su Y.-F., Ball C. D., Smith B. T., Cox R., Steinke R., McDaniel P. and Wasserzug L. (2013) Adapting Raman Spectra from Laboratory Spectrometers to Portable Detection Libraries. *Appl. Spectrosc.* **67**, 149–157.

Williams S. D., Johnson T. J., Gibbons T. P. and Kitchens C. L. (2007) Relative Raman Intensities in C_6H_6, C_6D_6, and C_6F_6: A Comparison of Different Computational Methods. *Theor. Chem. Acc.* **117**, 283–290.

Winkler, L.W. (1888). Die Bestimmung des in Wasser gelösten Sauerstoffen. Berichte der Deutschen Chemischen Gesellschaft, 21: 2843–2855.

Youker A. J., Krebs J. F., Hebden A., Quigley K., Stepinski D. and Vandegrift G. F. (2012) *Van*

de Graaff Experiments: Mo Redox Chemistry and Iodine Speciation., Argonne, IL (United States).